Co single-atoms on ultrathin N-doped porous carbon by biomass complexation strategy for high performance metal-air batteries

Journal:	*Journal of Materials Chemistry A*
Manuscript ID	TA-ART-11-2019-012171.R1
Article Type:	Paper
Date Submitted by the Author:	13-Dec-2019
Complete List of Authors:	Wang, Yanqiu; Central South University, School of Chemistry and Chemical Engineering Yu, Baoying; Central South University, Xiangya School of Medicine Liu, Kang; Central South University, School of Physics and Electronics Yang, Xuetao; Central South University, School of Chemistry and Chemical Engineering Liu, Min; Central South University, School of Physics and Electronics Chan, Ting-shan; National Synchrotron Radiation Research Center Qiu, Xiaoqing; Central South University, School of Chemistry and Chemical Engineering Li, Jie; Central South University, School of Chemistry and Chemical Engineering Li, Wenzhang; Central South University, School of Chemistry and Chemical Engineering

SCHOLARONE™
Manuscripts

Journal Name

ARTICLE

Co single-atoms on ultrathin N-doped porous carbon by biomass complexation strategy for high performance metal-air batteries

Yanqiu Wang,[a] Baoying Yu,[d] Kang Liu,[c] Xuetao Yang,[a] Min Liu,[c] Ting-Shan Chan,[e] Xiaoqing Qiu,[a] Jie Li,*[a] and Wenzhang Li *[ab]

The sluggish kinetics of the air electrode largely limits practical applications of metal-air battery. At present, preparing single atom catalysts confined in ultrathin N-doped porous carbon (NPC) with a high surface area remains a challenge. Herein, a facile strategy by complexation of biomass and metal ions, combining gas-foaming method, was used to synthesize substantial $Co-N_4$ active sites on ultrathin NPC with super-high specific surface area of 1977.9 m^2 g^{-1}. The catalyst owns brilliant oxygen reduction reaction property with higher half-wave potential of 0.863 V and faster kinetics process (68.3 mV dec^{-1}) than Pt/C (0.856 V, 80.46 mV dec^{-1}). Remarkably, it exhibits distinguished reversibility with high beginning cycle efficiency of 60.8% and satisfactory stability under Zn-air batteries. Moreover, assembly Al-air battery displays preeminent discharge performance with ultrahigh power density (494 mW cm^{-2}) and energy density (2387 Wh kg^{-1}) at 200 mA cm^{-2}. This work opens a new avenue to fully utilize biomass for constructing Co single atom catalysts for metal-air battery.

1. Introduction

High capacity energy storage and conversion technologies with eco-friendliness and sustainability (such as metal-air batteries and fuel cells) play significant roles in the world.[1-6] Especially, metal-air batteries have been seen as an attractive choice of power source for the new-generation electrical vehicles (EVs) and wide application prospects in small electronic equipment, in virtue of corresponding high theoretical energy density, stable operating voltage and rich metal reserves.[7, 8] However, these metal-air batteries can not realize their full potential to the utmost extent because of the slow kinetics process of oxygen reduction and evolution reaction (ORR/OER) in air electrode.[9-11] Thus, the vital research direction is to seek highly efficient ORR/OER catalysts to improve performance of the metal-air battery.[12-16] Recently, tremendous endeavors have been taken to exploit advanced free-noble metal catalysts to replace Pt- or Ru-based materials.[17-21] Atomically dispersed catalysts (SACs) have stimulated new attention in the field of electro-catalysis attributed

to high catalytic performance, selectivity and full efficient utilization of atoms.[22-27] For instance, the $M-N_4$ (M represents Co or Fe) structure of M-N-C acts as vital active spots for O_2 adsorption and later fracture of O=O bond during the ORR procedure,[5, 25, 28] which can reduce the activation barriers of cathode reaction. However, there is a gap between utilization efficiency of active metal sites and theory values. These ORR and OER occur at three-phase interface,[29] where only the revealed active sites can be beneficial for reactions. Therefore, exploring bi-functional single atom catalysts with improved utilization of active spots at reaction interface remains a serious challenge by suitable methodology.

At present, wet chemistry approaches have been widely used to fabricate SACs, which own great promising future in satisfying the requirement of practical energy storage application. However, they are easy to agglomerate and form nanoparticles in the conventional wet impregnation, causing loss of active sites and decay of catalytic activity. In addition, the preparation methods of SACs include photochemical reduction,[30] ion exchange,[31] surface modification[32] and so on. The low metal loading content for SACs largely limits practical applications in metal-air battery. For instance, a general carbon matrix has low density of targeted sites to lock metal ions and small surface area, which impedes wide application of M-N-C catalysts. Additionally, there is weak interaction between metal ions and carbon carrier, causing agglomeration of metal atoms into nanoparticles. Therefore, constructing intense interaction between metal precursors and substrate or ligand possesses vital effect on fabrication of SACs. For an appropriate substrate, it not only requires generous anchoring sites and reveals active spots at the reaction interface, but also can be favor for rapid mass/electron transport.

[a.] School of Chemistry and Chemical Engineering, Central South University, Changsha, 410083, China. E-mail: liwenzhang@csu.edu.cn, lijieliu@csu.edu.cn; Tel./fax: +86-731-88879616

[b.] Hunan Provincial Key Laboratory of Efficient and Clean Utilization of Manganese Resources, Central South University, Changsha 410083, China

[c.] School of Physics and Electronics, Central South University, Changsha 410083, China.

[d.] Xiangya School of Medicine, Central South University, Changsha, 410083, China.

[e.] National Synchrotron Radiation Research Center, Taiwan, 101 Hsin Ann Road, Hsinchu Science Park, Hsinchu 300, Taiwan

Specially, ultrathin porous carbon construction indicates ultimate low-end limit for isolated Co-N$_x$ moieties, which increases surface area to expose rich active sites, shorten diffusion path and accelerate mass/electron transport in the reaction. The above traits of ultrathin carbon materials have been confirmed by employing N-doped graphene anchored single metal atom catalysts.[33] Yet, the reported prepared tactics mainly are wet impregnation with after-treatment or multiple step procedure. Therefore, developing reasonable, scalable and effective techniques is indispensable for fabricating SACs with ultrathin porous carbon carriers.

Herein, we controllably fabricate scalable Co single-atom anchored on N-doped 3D ultrathin porous carbon sheets catalyst via complexation of biomass and metal ions, combining gas-foaming strategy. The ultrathin hierarchically porous carbon with super high specific surface area of 1977.9 m^2 g^{-1} can supply generous anchoring points for capturing metal atoms, which endows high density active sites of Co-N$_4$ for prepared Co SANC-850, making for fast diffusion of mass and electron on the electrochemical boundary. The single atom Co catalyst shows excellent ORR performance, achieving higher half-wave potential and faster kinetics rates than Pt/C. Applying Co SANC-850 catalyst as air cathode in Al-air battery, it exhibits excellent super high peak power density, impressive energy density and excellent stability under high current density. Furthermore, Co SANC-850 demonstrates excellent ORR/OER performance, stability and cycle efficiency in rechargeable Zn-air battery.

2. Experimental procedures

2.1 Preparation of Co SANC

Firstly, 1.0 g of chitosan, 5 g of NH$_4$Cl, 0.1 mmol of Co(Ac)$_2$·4H$_2$O and 1 mL HAc were added into 50 mL of deionized water to form a transparent solution under stirring for 30 min. Then, the mixture was vacuum freeze-dried for 12 h and the obtained solid mixture was calcination for 2 h under Ar atmosphere at 850 °C (750, 800 and 900 °C). The synthetic product was pickled by 2 M HCl for 12 h at room temperature. It was labeled as Co SANC-x (x represents temperature) catalyst. For comparison, Co SANC-850-0 and NC-850 were obtained via above same way without addition of NH$_4$Cl and metal salt, separately.

2.2 Electrochemical measurements

All electrochemical tests were conducted on a three-electrode system, which contained reference electrode (Hg/HgO), counter electrode (graphite rod) and working electrode with diameter of 5 mm (rotating disk electrode, RDE). The uniform catalyst dispersive ink was gained by decentralizing 4 mg sample powders into 990 µL of ethanol (98 vol%) and 10 µL of Nafion (5 wt%) under sonication for 30 min. For purposes of comparison, commercial Pt/C (20 wt%) catalyst dispersing solution was obtained in the same way as above. Followed by, 10 µL of homogeneous catalytic dispersing solution was covered to a rotating disk electrode and dried in atmosphere, provided with a catalyst content of around 0.2 mg cm^{-2}. The ORR and OER experiments were implemented in 0.1 M KOH after purging with O$_2$ gas for 30 min. All the potentials were converted to the reversible hydrogen electrode (RHE).

2.3 Fabrication of metal-air battery

The air cathode for the metal-air battery included three layers: catalytic layer, nickel foam and gas diffusion layer (GDL). The catalytic layer (CL) was prepared via rolling press by mixing catalyst, conductive additive (ketjen black, ECP-600JD) and acetylene black) and binder (polytetrafluoroethylene emulsion, PTFE, 60 wt%) uniformly in appropriate absolute ethanol (mass ratio: 3:3:1:3). The active area of air-electrode was 1x1 cm^2 with catalyst content of 2.0 mg. The GDL was obtained according to the above method using the acetylene black and PTFE (mass ratio: 1:3). The entire thickness of structure was 0.3 to 0.4 mm after completing installing air electrode. The polished Al and Zn plates were used as the anode. The composition of the electrolyte includes 6 M KOH, 0.01 M Na$_2$SnO$_3$, 0.5 mM In(OH)$_3$ and 7.5 mM ZnO for the Al-air battery. The electrolyte of Zn-air battery was composed of 6 M KOH and 0.2 M Zn(Ac)$_2$ to guarantee the reversibility of Zn electrode reaction.[34] Finally, the Al-air and Zn-air batteries were home-made by air cathode and corresponding metal plates. All battery performance tests were conducted on LAND CT2001C testing system at room temperature.

3. Results and discussion

3.1 Fabrication and characterization of catalysts

In the synthesis process of catalyst, we utilized chitosan (rich resource) with -NH$_2$ and -OH as chelating agent to coordinate with metal ions (Co^{2+}) uniformly.[35, 36] Meanwhile, NH$_4$Cl salt acted as gas-foaming agent to construct 3D carbon materials with ultrathin sheets structure.[37] Under the pyrolysis process, NH$_4$Cl could be resolved into gases of NH$_3$ and HCl, promoting the formation of ultrathin carbon sheets and porous texture. Followed by acid picking to eliminate residual salts and produced nanoparticles, the Co SANC catalyst was gained. A facile tactic by complexation of biomass and metal ions, combining gas-foaming method can be applied to prepare scalable materials along with good reproducibility based on coordination effects of chitosan with metal ions. These functional groups of chitosan can efficiently impede the metal atoms from aggregation and improve dispersion of metal atoms during carbonization, making Co in situ trapped with surrounding nitrogen to generate Co-N$_4$ structure because nitrogen with lone-pair electrons can strongly coordinate with Co atoms [38], which is conducive to enhancing stability of active sites. At present, there are still challenges for constructing 3D ultrathin N-doped porous carbon architectures with high specific surface area derived from biomass precursors and concurrently possessing abundant anchoring points for capturing single metal atoms. Here, under the procedure of synthesizing materials, addition of NH$_4$Cl (gas-foaming agent) plays a vital role in controlling microstructure of final sample. Without the addition of NH$_4$Cl, the SEM image of catalyst displays irregular carbon plate construction with a few cavities on its surface in Figure S1a. When employing NH$_4$Cl as foaming agent, in Figure 1a, b and Figure S1b, the SEM images of Co SANC-850 reveal that it presents fluffy 3D structure with homogeneous morphology consisted of 2D carbon sheet and massive pore, and no obvious Co nanoparticles can be

seen on the surface,[35] making reactant (electrolyte and oxygen) more accessible to active sites of catalyst. [39] As magnified SEM images in Figure 1c and Figure S1c, the Co SANC-850 was made of ultrathin interconnected carbon sheets. The atomic force microscope (AFM) images demonstrate that the thickness of the nanosheets for Co SANC-850 is 1.086 nm (Figure S4a-c), confirming the significant impact of NH_4Cl on the formation of ultrathin carbon structure. The corresponding TEM images show the loose material with ultrathin sheets structure and Co nanoparticles or clusters are not detected (Figure 1d and e). The structure merits of Co SANC-850 can accelerate electron transmission kinetics and afford rich active sites, which are great contribution to elevating oxygen reaction activity. The Co content of 1.27 wt% in the Co SANC-850 is detected by the coupled plasma optical emission spectrometry analysis.[32, 40] Employing aberration-corrected HAADF-STEM (Figure 1f), the homogeneous distribution of individual Co atoms (signed as red circle) is revealed in a porous carbon matrix because of the sensitive Z-contrast of heavy elements. [38]

A series of products were synthesized at different carbonization temperature in order to explore derivation of morphology and structure for Co SANC materials. Under a relatively low pyrolysis temperature of 750 °C, only large carbon sheets can be gained for Co SANC-750 (Figure S1d and e), which is consistent with the result of TEM (Figure S2a-c) and has the corresponding thickness of 6.271 nm

(Figure S4d-f). When the annealing temperature reached up 800 °C, interconnected 3D porous carbon structure is detected (Figure S1f and g), which is similar to architecture of Co SANC-850 sample. The corresponding TEM images confirm the existence of 2D carbon sheets (Figure S2d-f). The AFM images distinctly express that the thickness of Co SANC gradually decreases from 750 to 850 °C (Figure S4). However, a slight collapsed structure can be observed from SEM images (Figure S1h and i) for Co SANC-900, which also can be confirmed by increased nanosheets thickness and reduced specific surface area in comparison with Co SANC-850 (Figure S3a). The above results show that the carbonization temperature plays a crucial role in controlling morphological and structure evolution for Co SANC materials. Meanwhile, in the synthetic samples, the Co SANC-850 exhibits N-doped ultrathin porous carbon structure with the largest specific surface area of 1977.9 $m^2 g^{-1}$ and pore volume of 2.99 $m^3 g^{-1}$ than that of Co SANC-750 (376 $m^2 g^{-1}$ and 2.99 $m^3 g^{-1}$), Co SANC-800 (720 $m^2 g^{-1}$ and 0.37 $m^3 g^{-1}$) and Co SANC-900 (1446 $m^2 g^{-1}$ and 1.95 $m^3 g^{-1}$). The high specific surface area and large pore volume have a vital part in offering more appearance of active sites and accelerating mass transport during the reaction process due to existence of hierarchical pore textural containing some micropores, mesopores and fewer macropores (Figure S3), guaranteeing that the kinetics process of oxygen reaction is enhanced.
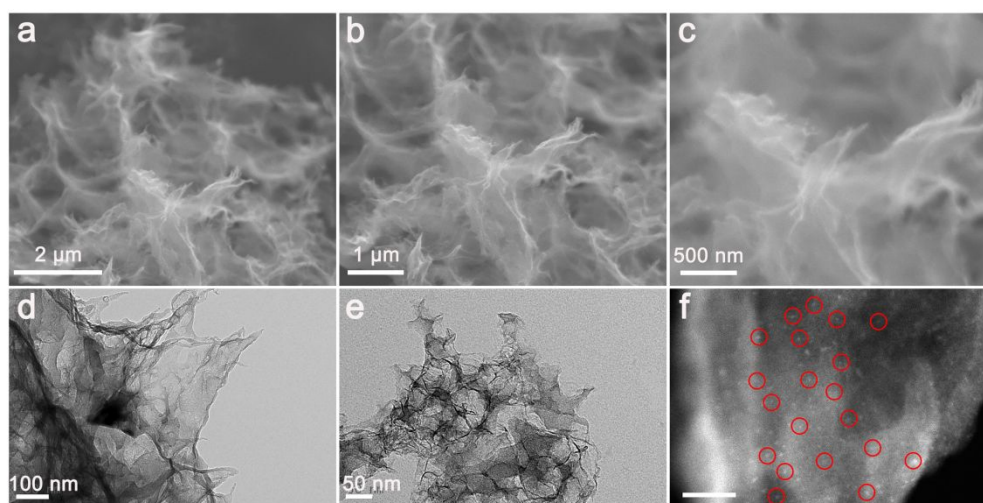

Figure 1 (a-c) SEM images, (d, e) TEM images and (f) Aberration-corrected HAADF image, scale bar, 10 nm, for the Co SANC-850 on the carbon support.

The X-ray powder diffractometer (XRD) patterns and Raman spectra were carried out to investigate the metal and carbon crystalline structure for the as-obtained catalysts. The CoSANC-850 and other samples show no peaks of cobalt species and a wide diffraction peak around 24.7° is obtained (Figure S5), corresponding to (002) plane of hexagonal graphite carbon.[5, 41] There are no additional peaks related to cobalt species, in good agreement with results of HRTEM analysis, demonstrating that Co atoms are anchored on N-doped carbons materials. Meanwhile, Raman spectroscopy tests were also implemented to further study the

structural information of these catalysts. The two characteristic Raman peaks of D band and G band appear at 1335 cm^{-1} and 1594 cm^{-1} (Figure 2a), which are related to disordered carbon and sp2-hybridized graphitic carbon structure, independently. Their intensity specific ratios (I_D/I_G) represent graphitization degree and the level of disorder of carbon materials. In addition, the Raman spectra were fitted into four peaks (D1, D3, D4 and G)[42] in Figure 2b and Figure S6a-c. Specifically, D1 peak is assigned to edge plane defects, D3 is related to amorphous carbon and D4 is corresponded to polyene-like architecture or introduction of ionic impurities.[43] The I_{D1}/I_G intensity

value of Co SANC-850 (2.05) is higher than other samples except for Co SANC-900 (Figure 2c), implying that the Co SANC-850 can possess more defects structure for improving O_2 adsorption ability[44, 45] and promoting the ORR activity.[46] However, the Co SANC-900 can possess maximum I_{D1}/I_G value due to its collapsed structure, in accord with the results of SEM and reduced SSA of Co SANC-900.

XPS (X-ray photoelectron spectroscopy) spectra were applied to examine the surface composition and electronic structures of Co SANC. Figure 2d distinctly displays the existence of C, O, N, and Co elements for Co SANC. The metal contents from XPS and ICP-OES measurements were determined (Table S1). In Figure 2e, high-resolution Co 2p spectrum clearly demonstrates two major peaks with Co 2$p_{1/2}$ (780.4 eV) and Co 2$p_{3/2}$ (796.1 eV), and related satellite peaks (784.9 eV), which is ascribed to Co-N bonding.[47] The above result clearly reveals the formation of Co-N sites and eliminates the presence of metallic state in the samples, which are the effective sites for catalyzing oxygen reduction reaction.[48] Acquired from the high-resolution XPS C 1s spectrum of Co SANC (Figure S6d), C types can be mainly divided into four peaks: C=C (sp^2, 284.7 eV), C-N (285.8 eV), C-O (287.3 eV) and C=O (291.0 eV),[49] which is created by the importation of oxygen-including functional groups in synthetic Co SANC procedure. Carbon atoms of sp^2-hybridized composition are existent in the samples, consistent with the result of Raman spectra. Furthermore, there are C-O and C=O groups for fine-resolution O 1s spectra of samples in Figure S6e. These electron-withdrawing groups can regulate the charge distribution of neighboring carbon atoms, which can boost the adsorption of intermediate for ORR and OER. The fine-resolution N 1s spectra (Figure 2f) can be classified into five peaks lying at 398.3, 399.2, 399.9, 401 and 402-406 eV, related to pyridinic N, Co-N$_x$, pyrrolic N, graphitic N and oxidated N, respectively. Evidently, pyridinic N and graphitic N are the primary peaks, which make for ORR performance. In addition, pyridinic N can act as anchor points to disperse single Co atoms equably.

X-ray absorption fine structure spectroscopy investigations were implemented to further ascertain cobalt atomic structures for Co SANC-850 catalyst. Figure 3a shows the normalized X-ray absorption near edge structure spectra of samples. A relatively smooth curve is observed in the Co SANC-850 comparing with reference such as Co-foil, CoO and Co_3O_4. The location of edge of Co SANC-850 is situated between the CoO and Co_3O_4, distinctly manifesting that Co oxidation in the catalyst is situated between Co (II) and Co (III). The Fourier transformation EXAFS spectroscopy about the Co SANC-850 (Figure 3b) clearly exhibits a vital peak at about 1.40 Å, different from Co-O bond peak at 1.75 Å (CoO), 1.57 Å
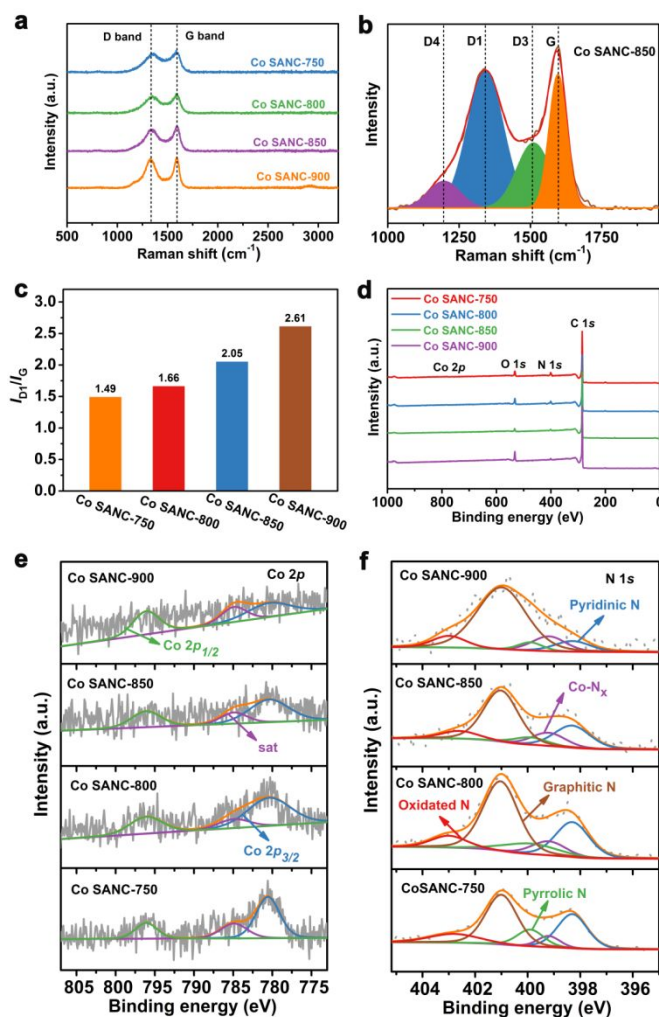

Figure 2 (a) Raman spectra for Co SANC-750, Co SANC-800, Co SANC-850 and CoSANC-900. (b) the fitting outcome of Raman spectrum for Co SANC-850, (c) intensity ratio of I_{D1}/I_G, (d) XPS spectra, (e) Co 2p and (f) N 1s High-resolution XPS spectra for Co SANC-750, Co SANC-800, Co SANC-850 and Co SANC-900.

(Co_3O_4) and Co-Co bond peak at 2.18 Å (Co-foil), which is assigned to Co-N structure scattering path.[50] The results confirm that the Co atoms are atomically dispersed in nitrogen doped carbon materials. Meanwhile, the coordination number of Co-N structure of Co SANC-850 is quantified via least-squares EXAFS plot fitting. According to the well-matched EXAFS fitting outcomes of Co SANC-850 (Figure 3c and Table S2), the coordination number of the Co-N centers is 4 with simulative distance of 1.878 Å, which is consistent with reported literature.[51] Moreover, fine-resolution N 1s spectrum of Co SANC-850 testifies generation of Co-N structure at 399.2 eV, acting as a side testimony of XAS outcomes. Thus, these results obviously demonstrated coordination environment of isolated Co sites in the Co SANC-850 catalyst.
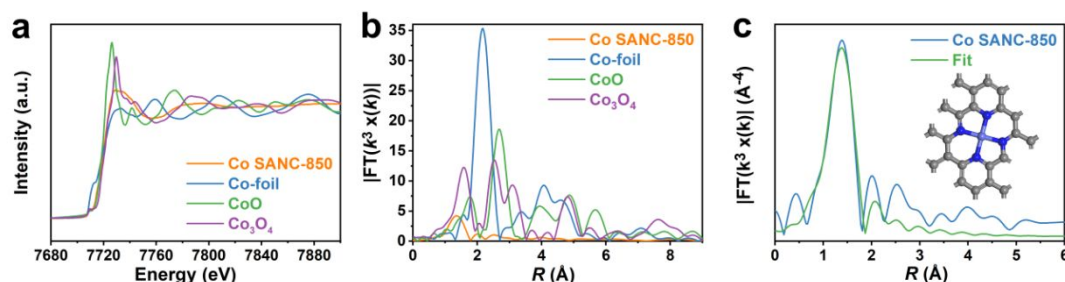
Figure 3 (a) Co K-edge XANES spectra, (b) Fourier transformed (FT) k^3-weighted χ (k)-function of the EXAFS spectra for Co K-edge of Co SANC-850 and reference sample. (c) typical EXAFS fitting curves of Co SANC-850 at R space, insert schematic model of Co SANC-850, Co (pale blue), N (blue) and C (gray).

3.2 Electrochemical property

Selecting the ORR as goal response estimated the catalytic activity of the as-designed catalysts, because of a current obstacle of metal-air batteries about sluggish kinetics of cathode. The ORR performance tests were implemented in 0.1 M KOH solutions (O_2-saturated) via cyclic voltammogram (CV) and linear sweep voltammetry (LSV). The obvious oxygen reduction peak potential of Co SANC-850 is closed to Pt/C (Figure S7). Furthermore, Figure 4a and

b distinctly certify that Co SANC-850 exhibits satisfying activity in the aspect of both positive onset potential (E_{onset}, 0.995 V) and half-wave potential ($E_{1/2}$, 0.863 V) than that of other prepared catalysts. The boosted ORR activity of Co SANC-850 is mainly attributed to the formation of effective Co-N_4 active sites in contrast to metal-free NC-850 sample,[28] which are beneficial to O_2 adsorption and O=O break subsequently, testifying the vital role of atomically dispersed Co atoms as for improving ORR activity.
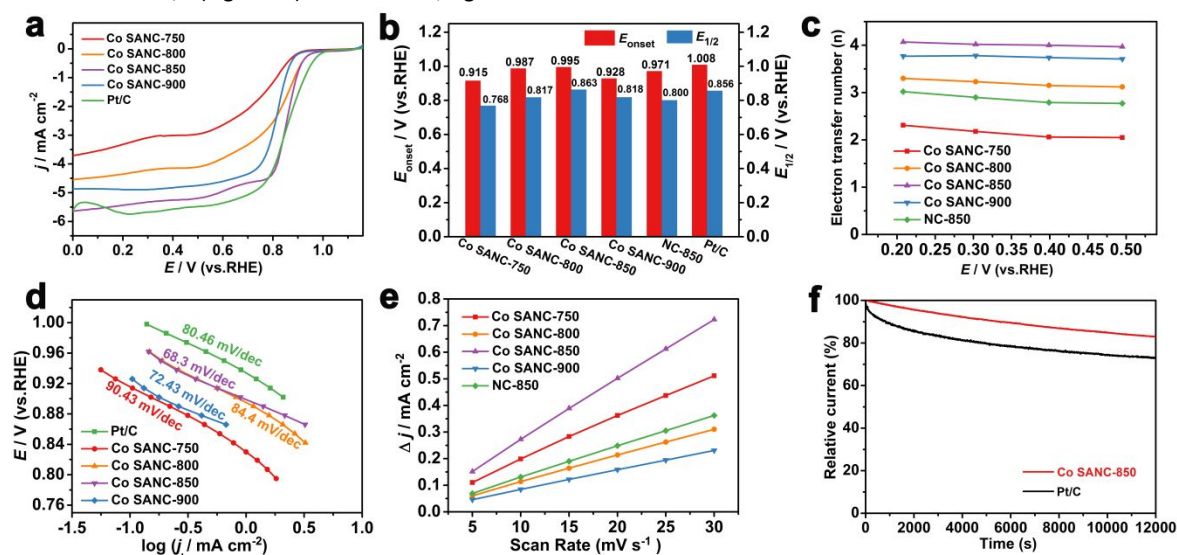

Figure 4 (a) LSV curves of samples, (b) onset potentials and half-wave potential, (c) electron transfer numbers (n), (d) Tafel plots, (e) CV fitting curve of catalysts at 1.057 V and (f) stability test for Co SANC-850 and Pt/C at 0.667 V vs RHE.

The polarization curves of Co SANC and NC-850 materials with different rotation rates were applied to study the ORR mechanism in depth. In accordance with LSV curves (Figure S8 and Figure S9a) at diverse rotation speeds and Koutecky-Levich (K-L) equation,[52-54] we calculated electron transfer number of ORR in these catalysts for single oxygen molecule. The K-L plots at distinct imposed potentials are revealed (Figure S8 and Figure S9b). The calculated average electron transfer numbers (n) of Co SANC-850 is about 4.02, which has much higher value than that of other catalysts (Figure 4c), indicating a clear 4e- process toward ORR approaching to the Pt/C. The K-L plots disclose almost parallelism and fitting linear

characteristic, reflecting the first-order reaction kinetics with regard to dissolving O_2. [46, 55, 56]

Tafel slope is usually used to effectively evaluate the kinetic property of electrocatalytic reaction. As shown in Figure 4d and Figure S9c, Co SANC-850 exhibits the smallest Tafel slope of 68.3 mV dec^{-1} than that of Co SANC-750 (90.43 mV dec^{-1}), Co SANC-800 (84.4 mV dec^{-1}), NC-850 (90.2 mV dec^{-1}), Co SANC-900 (72.43 mV dec^{-1}) and Pt/C (80.46 mV dec^{-1}). The above results demonstrate a quick kinetics process for the Co SANC-850 compared to Pt/C. Furthermore, electrochemical active surface area (ECSA) was assessed by CV investigations from 1.007 V to 1.107 V (vs RHE) in Figure S10, which could be expressed via the double layer capacitance. [6, 24, 57] Co SANC-

850 displayed a higher ECSA than other samples in Figure 4e, confirming that Co SANC-850 afforded higher density revealed active sites and more distinguished ORR performance than contrast sample. The electrochemical impedance spectroscopy (Figure S9d) present that Co SANC-850 possesses a smaller charge transfer resistance comparing with Pt/C and prepared catalysts, evidently suggesting that Co SANC-850 has excellent conductivity and better charge transport performance.[58]

Furthermore, the OER property of catalyst was appraised in 0.1 M KOH solution via 1600 rpm. As shown in Figure S11a, Co SANC-850 presents a smaller over-potential than Pt/C, approaching to that of RuO_2 at current density of 10 mA cm^{-2}. Importantly, Co SANC-850 delivers larger current density under high potential and smaller Tafel slope of 286 mV dec^{-1} than that of Pt/C (368 mV dec^{-1}), inferior to RuO_2 (135 mV dec^{-1}) in Figure 11b, demonstrating that Co SANC-850 owns quicker transport process of mass and electron than Pt/C on the electrochemical reaction boundary. The above outcomes indicate that Co SANC-850 can act as a prospective ORR/OER catalyst for rechargeable metal-air battery.

Except for excellent catalytic activity, the stability of Co SANC-850 was investigated by chronoamperometric tests at 0.667 V (vs. RHE). The Co SANC-850 shows more robust stability than Pt/C for ORR in alkaline medium after 12000 s reaction (Figure 4f). In fact, TEM and ICP-OES measurements were carried out to study the changes of morphology and Co content before and after reaction. In Figure S12, TEM images corroborated that Co SANC-850 maintains original ultrathin carbon structure and there is no Co nanoparticles or clusters after catalysis. Importantly, the content of cobalt in electrolyte was not detected after catalysis by the ICP-OES measurement. The above outcomes confirm that Co SANC-850 owns good immunity to aggregation and dissolution in catalysis process.

3.3 Theoretical calculation

To inquiry the origin for the excellent ORR/OER activity of Co SANC-850, DFT calculations were carried out to estimate the role of quantified $Co-N_4$ configuration (Figure 3c, EXAFS fitting curves), comparing to pyridinic N and graphitic N models (Figure 5a-c). The DFT calculations method and simulation details can be seen in theoretical section, Figure S17 and Table S3-S12 in the Supporting Information. Generally, the catalyst with smaller over-potential can offer higher catalytic activity. For the ORR, free energy of each elementary reaction steps for $Co-N_4$, graphitic N and pyridinic N is downhill at U= 0 V (Table S7) in Figure 5d. Furthermore, under equilibrium potential of 1.23 V, some elementary reactions aren't thermodynamically favorable on the three sites in Figure 5f and Table S8, where the generation of *OOH, production and releasing of *OH are steps of free energy rising. Importantly, $Co-N_4$ affords smaller energy barriers relative to graphitic N and pyridinic N under those steps. When the potential is reduced to 0.98 V, the free energy change of the last reaction step (release of *OH) for $Co-N_4$ is zero, but the other elementary reactions remain downhill (Figure 5h), which indicates that last elementary reaction step with charge transfer is rate-limiting step for ORR. Hence, the U_{RHE} = 0.98 V is the limiting potential of $Co-N_4$ sites, which is higher than the graphitic N (0.7 V)

and pyridinic N (0.3V), indicating higher activity for $Co-N_4$ with minimum over-potential of 0.25 V, compared with the other two sites (Table S9). The corresponding reaction mechanism of OER was gained from DFT calculations (Figure 5e, g and i). Figure 5e presents that the free energy of every reaction is uphill at potential of 0 V (Table S10). At U=1.23 V, the production and release of *O are endothermic steps on $Co-N_4$ active site (Figure 5g). In addition, some elementary reactions aren't thermodynamically favorable on the graphitic N and pyridinic N (Table S11). In Figure 5i and Table S12, the transformation of *OH to *O is limiting step with largest energy change (U=1.64 V, $Co-N_4$). The related over-potential is 0.45 V, which is the minimum than those of graphitic N (0.69 V) and pyridinic N (1.25 V).The above results confirm that $Co-N_4$ structure is vital contributor to highly efficient ORR and OER for Co SANC-850.
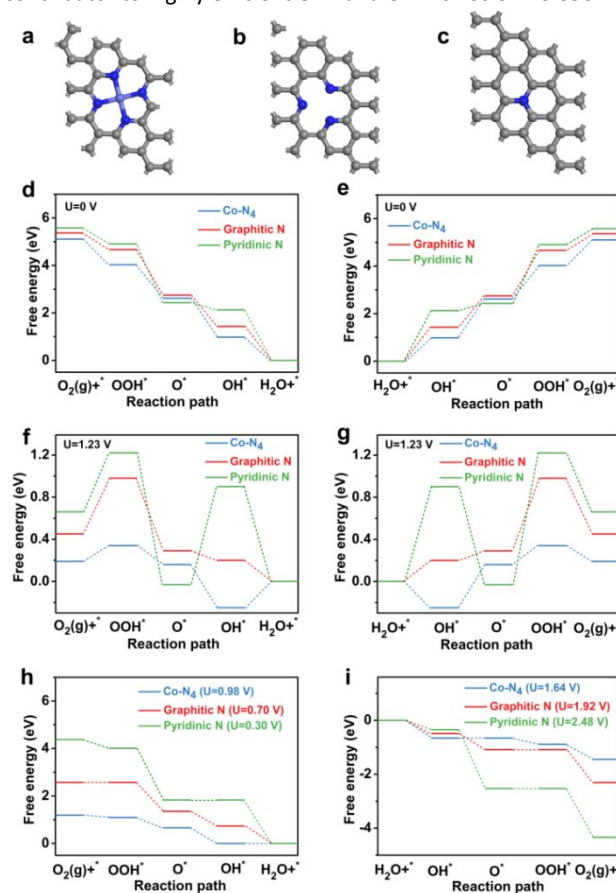
Figure 5 Computational models of (a) $Co-N_4$, (b) Pyridinic N and (c) Graphitic N. (d-i) free energy diagram for ORR and OER on $Co-N_4$, Graphitic N and Pyridinic N at different electrode potential, respectively.

3.4 Al-air and Zn-air batteries

Furthermore, we fabricated metal-air batteries applying Co SA NC-850 with outstanding ORR activity as the air cathode catalyst. The home-made Al-air battery possesses a high open circuit voltage reaching up to 1.80 V, which overmatches Co SANC-800 (1.76 V), NC-850 (1.66 V), comparable to Pt/C (1.82 V) in Figure S13 and Figure S15a. Figure 6a reveals the discharge polarization plots and the according power density, displaying the excellent peak power density of 494 mW cm^{-2} than that of Pt/C (449 mW cm^{-2}), Co SANC-

800 (426.8 mW cm^{-2}), NC-850 (344 mW cm^{-2}) and the reported advanced Al-air batteries (Figure S15b and Table S13). And the Co SANC-850 holds smaller discharge over-potential than that of Pt/C, Co SANC-800 and NC-850 in Al-air battery operation. In addition, the corresponding steady plots of long-term constant current densities discharge reveal no evident voltage decay for 10 h, confirming good catalytic stability of Co SANC-850 catalyst (Figure 6b). The discharge voltage of Co SANC-850 is comparable to Pt/C at 10 mA cm^{-2} and 50 mA cm^{-2} as pictured in Figure S14, due to excellent ORR performance for Co SANC-850. Based on normalized the weight of the consumed aluminum, the corresponding specific capacity and energy density were gained for the Co SANC-850 comparable with Pt/C at diverse discharge current densities. More importantly, Co SANC-850 exhibits remarkable specific capacity, energy density and higher discharge voltage even at high current density of 200 mA cm^{-2} than that of Co SANC-800, NC-850 and Pt/C in Figure 6c, d and Figure S15c, d, which are attributed to the merits of the uniform dispersion of Co-N$_4$ active sites on 3D porous carbon materials and hierarchically ultrathin pore textural (with a high surface area) favoring fast mass/electron transfer on electrochemical reaction interface for Co SANC-850.
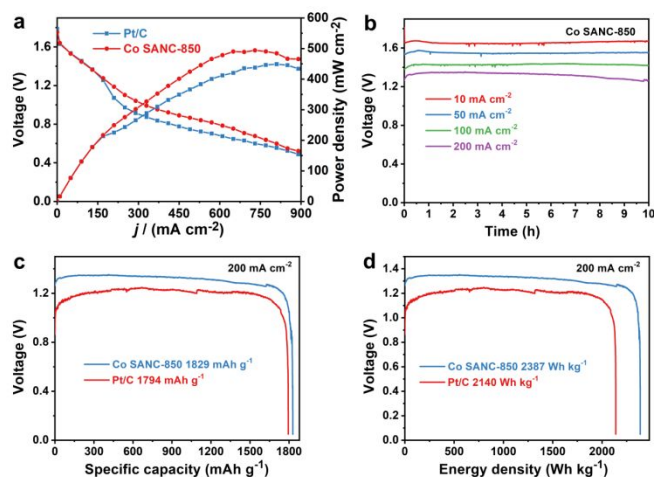

Figure 6 (a) Polarization and power density plots, (b) long-time discharge curves at different discharge densities, (c) specific capacities, (d) energy densities under 200 mA cm^{-2} of Al-air battery.

For assessing the latent application in rechargeable device, a secondary and primary Zn-air battery were equipped with zinc anode, alkaline electrolyte and air cathode. As shown in Figure 7a, Co SANC-850 affords higher open circuit voltage of 1.48 V compared to Pt/C (1.45 V) in the primary Zn-air battery. In addition, Co SANC-850 delivers a specific capacity of 860.95 mAh g^{-1} based on the weight of consumptive Zn plate, which overmatches the contrast battery with Pt/C of 790.12 mAh g^{-1} at 10 mA cm^{-2} in Figure S16. For a rechargeable Zn-air battery system, Figure 7b displays the discharge-charge polarization plots of Co SANC-850 and Pt/C+RuO$_2$, reflecting that Co SANC-850 owns splendid rechargeable capacity as bifunctional catalyst. Noticeably, the higher electrochemical activity

for Co SANC-850 than Pt/C+RuO$_2$ was demonstrated by Zn-air battery test, which is distinct from the results of RDE measurement, attributed to their diversity of test condition. For the robustness of discharge-charge cycling investigations, Co SANC-850 has initial charging voltage of 1.99 V and discharge voltage of 1.21 V under 10 mA cm^{-2}, which slightly excels that of Pt/C+RuO$_2$ (2.0 V and 1.21 V) with a voltage gap of 0.79 V under same testing condition. The Co SANC-850 displays higher beginning cycle efficiency of 60.8% than Pt/C+RuO$_2$ (60.5%). In addition, Co SANC-850 displays a fascinating stability with nearly unchanged voltage gap after around 44 h cycles test. The discharge-charge performance of Zn-air battery applying Co SANC-850 as air electrode catalyst is comparable to the reported advanced Zn-air batteries (Table S14). The above results indicate that the Co SANC-850 has great application prospects in the metal-air battery.
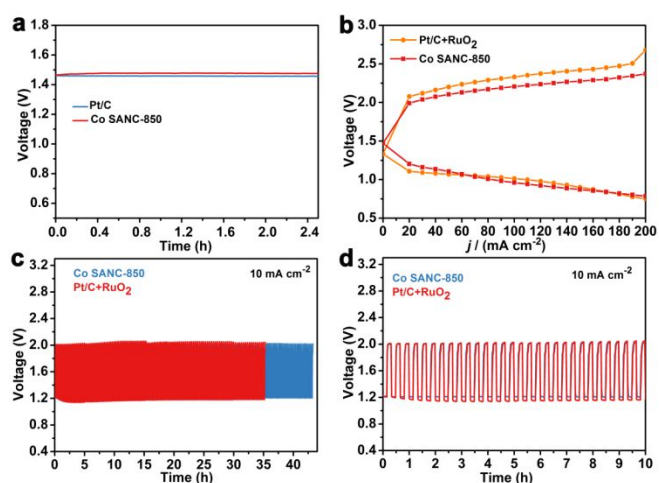

Figure 7 (a) open-circuit voltages, (b) charge and discharge polarization plots and (c, d) cycling curves for rechargeable Zn- air battery at 10 mA cm^{-2} under 20 min per cycle.

4. Conclusion

In conclusion, we have proposed the well-distributed single-atom Co catalyst with Co-N$_4$ structure anchored on ultrathin 3D N-doped porous carbon material by complexation of biomass and metal ions, combining gas-foaming strategy, which makes for catching oxygen species and accelerating oxygen reaction kinetics course. The designed Co SANC-850 has glorious catalytic activity and stability compared with Pt/C. The DFT calculations prove that Co-N$_4$ structure can promote ORR and OER activity. Importantly, the fabricated Al-air battery demonstrates splendid discharge performance with superb energy density of 2387 Wh kg^{-1} and weak polarization under 200 mA cm^{-2}, which precedes ever reported metal-air batteries. Meanwhile, Co SANC-850 exhibits outstanding open circuit voltage, cycle efficiency and stability in Zn-air battery. This high performance is attributed to the atomically dispersed Co-N$_4$ sites and excellent mass transport of hierarchically porous architecture at electrochemical boundary. This research provides a new guidance for promoting practical application of high-efficiency and stable metal-air batteries.

Conflicts of interest

There are no conflicts to declare.

Acknowledgements

Notes and references

1. Y. Zhao, L. P. Wang, M. T. Sougrati, Z. Feng, Y. Leconte, A. Fisher, M. Srinivasan and Z. Xu, *Adv. Energy Mater.*, 2017, **7**, 1601424.
2. I. S. Amiinu, X. Liu, Z. Pu, W. Li, Q. Li, J. Zhang, H. Tang, H. Zhang and S. Mu, *Adv. Funct. Mater.*, 2018, **28**, 1704638.
3. F. Meng, H. Zhong, D. Bao, J. Yan and X. Zhang, *J. Am. Chem. Soc.*, 2016, **138**, 10226-10231.
4. Y. Liu, F. Chen, W. Ye, M. Zeng, N. Han, F. Zhao, X. Wang and Y. Li, *Adv. Funct. Mater.*, 2017, **27**, 1606034.
5. X. X. Wang, D. A. Cullen, Y. T. Pan, S. Hwang, M. Wang, Z. Feng, J. Wang, M. H. Engelhard, H. Zhang, Y. He, Y. Shao, D. Su, K. L. More, J. S. Spendelow and G. Wu, *Adv. Mater.*, 2018, **30**, 1706758.
6. X. F. Lu, Y. Chen, S. Wang, S. Gao and X. W. Lou, *Adv. Mater.*, 2019, **31**, 1902339.
7. J. Ryu, H. Jang, J. Park, Y. Yoo, M. Park and J. Cho, *Nat. Commun.*, 2018, **9**, 3715-3724.
8. J. Ryu, M. Park and J. Cho, *Adv. Mater.*, 2019, **31**, 1804784.
9. W. Xia, A. Mahmood, Z. Liang, R. Zou and S. Guo, *Angew. Chem., Int. Ed.* , 2016, **55**, 2650-2676.
10. Z. Liu, J. Yu, X. Li, L. Zhang, D. Luo, X. Liu, X. Liu, S. Liu, H. Feng, G. Wu, P. Guo, H. Li, Z. Wang and X. S. Zhao, *Carbon*, 2018, **127**, 636-642.
11. T. He, Y. Zhang, Y. Chen, Z. Zhang, H. Wang, Y. Hu, M. Liu, C.-W. Pao, J.-L. Chen, L. Y. Chang, Z. Sun, J. Xiang, Y. Zhang and S. Chen, *J. Mater. Chem. A*, 2019, **7**, 20840-20846.
12. W. Zang, A. Sumboja, Y. Ma, H. Zhang, Y. Wu, S. Wu, H. Wu, Z. Liu, C. Guan, J. Wang and S. J. Pennycook, *ACS Catal.*, 2018, **8**, 8961-8969.
13. X. Lyu, G. Li, X. Chen, B. Shi, J. Liu, L. Zhuang and Y. Jia, *Small Methods*, 2019, 1800450.
14. X. Han, X. Ling, Y. Wang, T. Ma, C. Zhong, W. Hu and Y. Deng, *Angew. Chem., Int. Ed.* , 2019, **58**, 5359-5364.
15. Z. Li, M. Shao, Q. Yang, Y. Tang, M. Wei, D. G. Evans and X. Duan, *Nano Energy*, 2017, **37**, 98-107.
16. J. Li, J. Chen, H. Wan, J. Xiao, Y. Tang, M. Liu and H. Wang, *Appl. Catal., B*, 2019, **242**, 209-217.
17. Q. Zhao, Z. Yan, C. Chen and J. Chen, *Chem. Rev.*, 2017, **117**, 10121-10211.
18. Q. Li, R. Cao, J. Cho and G. Wu, *Adv. Energy Mater.*, 2014, **4**, 1301415-1301433.
19. S. Wei, A. Li, J. C. Liu, Z. Li, W. Chen, Y. Gong, Q. Zhang, W. C. Cheong, Y. Wang, L. Zheng, H. Xiao, C. Chen, D. Wang, Q. Peng, L. Gu, X. Han, J. Li and Y. Li, *Nat. Nanotechnol.*, 2018, **13**, 856-861.
20. J. Li, Z. Zhou, K. Liu, F. Li, Z. Peng, Y. Tang and H. Wang, *J. Power Sources*, 2017, **343**, 30-38.
21. Q. Hu, G. Li, G. Li, X. Liu, B. Zhu, X. Chai, Q. Zhang, J. Liu and C. He, *Adv. Energy Mater.*, 2019, **9**, 1803867.
22. J. Wang, Z. Li, Y. Wu and Y. Li, *Adv. Mater.*, 2018, **30**, 1801649.
23. T. Zheng, K. Jiang, N. Ta, Y. Hu, J. Zeng, J. Liu and H. Wang, *Joule*, 2019, **3**, 265-278.
24. Z. Liu, F. Sun, L. Gu, G. Chen, T. Shang, J. Liu, Z. Le, X. Li, H. B. Wu and Y. Lu, *Adv. Energy Mater.*, 2017, **7**, 1701154.
25. Y. Guo, P. Yuan, J. Zhang, Y. Hu, I. S. Amiinu, X. Wang, J. Zhou, H. Xia, Z. Song, Q. Xu and S. Mu, *ACS Nano*, 2018, **12**, 1894-1901.
26. L. Huang, J. Chen, L. Gan, J. Wang and S. Dong, *Sci. Adv.*, 2019, **5**, eaav5490.
27. Y. Peng, B. Lu and S. Chen, *Adv. Mater.*, 2018, **30**, 1801995.
28. H. Zhang, S. Hwang, M. Wang, Z. Feng, S. Karakalos, L. Luo, Z. Qiao, X. Xie, C. Wang, D. Su, Y. Shao and G. Wu, *J. Am. Chem. Soc.*, 2017, **139**, 14143-14149.
29. L. Zhao, Q. Wang, X. Zhang, C. Deng, Z. Li, Y. Lei and M. Zhu, *ACS Appl. Mater. Interfaces*, 2018, **10**, 35888-35895.
30. P. Liu, Y. Zhao, R. Qin, S. Mo, G. Chen, L. Gu, D. M. Chevrier, P. Zhang, Q. Guo, D. Zang, B. Wu, G. Fu and N. Zheng, *Science*, 2016, **352**, 797-800.
31. C. Zhao, X. Dai, T. Yao, W. Chen, X. Wang, J. Wang, J. Yang, S. Wei, Y. Wu and Y. Li, *J. Am. Chem. Soc.*, 2017, **139**, 8078-8081.
32. Y. Ye, F. Cai, H. Li, H. Wu, G. Wang, Y. Li, S. Miao, S. Xie, R. Si, J. Wang and X. Bao, *Nano Energy*, 2017, **38**, 281-289.
33. C. Zhang, J. Sha, H. Fei, M. Liu, S. Yazdi, J. Zhang, Q. Zhong, X. Zou, N. Zhao, H. Yu, Z. Jiang, E. Ringe, B. I. Yakobson, J. Dong, D. Chen and J. M. Tour, *ACS Nano*, 2017, **11**, 6930-6941.
34. H. Jiang, J. Gu, X. Zheng, M. Liu, X. Qiu, L. Wang, W. Li, Z. Chen, X. Ji and J. Li, *Energy Environ Sci.*, 2019, **12**, 322-333.
35. C. Zhang, S. Yang, J. Wu, M. Liu, S. Yazdi, M. Ren, J. Sha, J. Zhong, K. Nie, A. S. Jalilov, Z. Li, H. Li, B. I. Yakobson, Q. Wu, E. Ringe, H. Xu, P. M. Ajayan and J. M. Tour, *Adv. Energy Mater.*, 2018, **8**, 1703487-1703495.
36. Y. Chen, S. Ji, Y. Wang, J. Dong, W. Chen, Z. Li, R. Shen, L. Zheng, Z. Zhuang, D. Wang and Y. Li, *Angew. Chem., Int. Ed.* , 2017, **56**, 6937-6941.
37. X. Lu, K. Xu, P. Chen, K. Jia, S. Liu and C. Wu, *J. Mater. Chem. A*, 2014, **2**, 18924-18928.
38. Y. Qu, Z. Li, W. Chen, Y. Lin, T. Yuan, Z. Yang, C. Zhao, J. Wang, C. Zhao, X. Wang, F. Zhou, Z. Zhuang, Y. Wu and Y. Li, *Nat. Catal.*, 2018, **1**, 781-786.
39. H. T. Chung, D. A. Cullen, D. Higgins, B. T. Sneed, E. F. Holby, K. L. More and P. Zelenay, *Science*, 2017, **357**, 479-484.
40. K. Jiang, D. Zhao, S. Guo, X. Zhang, X. Zhu, J. Guo, G. Lu and X. Huang, *Sci. Adv.*, 2017, **3**, e1601705.
41. B. Lu, L. Guo, F. Wu, Y. Peng, J. E. Lu, T. J. Smart, N. Wang, Y. Z. Finfrock, D. Morris, P. Zhang, N. Li, P. Gao, Y. Ping and S. Chen, *Nat. Commun.*, 2019, **10**, 631.
42. Z. Chen, Q. Wang, X. Zhang, Y. Lei, W. Hu, Y. Luo and Y. Wang, *Sci. Bull.*, 2018, **63**, 548-555.

43.   J. Li, J. Chen, H. Wan, J. Xiao, Y. Tang, M. Liu and H. Wang, *Appl. Catal. , B*, 2019, **242**, 209-217.

44.   W. Liu, Y. Chen, H. Qi, L. Zhang, W. Yan, X. Liu, X. Yang, S. Miao, W. Wang, C. Liu, A. Wang, J. Li and T. Zhang, *Angew. Chem., Int. Ed.* , 2018, **57**, 7071-7075.

45.   C. Zhu, S. Fu, J. Song, Q. Shi, D. Su, M. H. Engelhard, X. Li, D. Xiao, D. Li and L. Estevez, *Small*, 2017, **13**, 1603407.

46.   L. Jiao, G. Wan, R. Zhang, H. Zhou, S. H. Yu and H. L. Jiang, *Angew. Chem., Int. Ed.* , 2018, **57**, 8525-8529.

47.   H. Zhang, W. Zhou, T. Chen, B. Y. Guan, Z. Li and X. W. Lou, *Energy Environ. Sci.*, 2018, **11**, 1980-1984.

48.   Q. Cheng, L. Yang, L. Zou, Z. Zou, C. Chen, Z. Hu and H. Yang, *ACS Catal.*, 2017, **7**, 6864-6871.

49.   Q. Wang, Y. Lei, Y. Zhu, H. Wang, J. Feng, G. Ma, Y. Wang, Y. Li, B. Nan, Q. Feng, Z. Lu and H. Yu, *ACS Appl. Mater. Interfaces*, 2018, **10**, 29448-29456.

50.   Y. Zhu, W. Sun, J. Luo, W. Chen, T. Cao, L. Zheng, J. Dong, J. Zhang, M. Zhang, Y. Han, C. Chen, Q. Peng, D. Wang and Y. Li, *Nat. Commun.*, 2018, **9**, 3861-3869.

51.   P. Yin, T. Yao, Y. Wu, L. Zheng, Y. Lin, W. Liu, H. Ju, J. Zhu, X. Hong, Z. Deng, G. Zhou, S. Wei and Y. Li, *Angew. Chem., Int. Ed.* , 2016, **55**, 10800-10805.

52.   Y. Han, Y. G. Wang, W. Chen, R. Xu, L. Zheng, J. Zhang, J. Luo, R. A. Shen, Y. Zhu, W. C. Cheong, C. Chen, Q. Peng, D. Wang and Y. Li, *J. Am. Chem. Soc.*, 2017, **139**, 17269-17272.

53.   H. Park, S. Oh, S. Lee, S. Choi and M. Oh, *Appl. Catal. , B*, 2019, **246**, 322-329.

54.   T. He, X. Wang, H. Wu, H. Xue, P. Xue, J. Ma, M. Tan, S. He, R. Shen, L. Yi, Y. Zhang and J. Xiang, *ACS Appl. Mater. Interfaces*, 2017, **9**, 22490-22501.

55.   P. Yin, T. Yao, Y. Wu, L. Zheng, Y. Lin, W. Liu, H. Ju, J. Zhu, X. Hong, Z. Deng, G. Zhou, S. Wei and Y. Li, *Angew. Chem., Int. Ed.*, 2016, **55**, 10800-10805.

56.   J. Wang, H. Zhang, C. Wang, Y. Zhang, J. Wang, H. Zhao, M. Cheng, A. Li and J. Wang, *Energy Storage Mater.*, 2018, **12**, 1-7.

57.   L. Bai, Z. Duan, X. Wen, R. Si and J. Guan, *Appl. Catal. , B*, 2019, **257**, 117930.

58.   Y. Peng, B. Lu, L. Chen, N. Wang, J. E. Lu, Y. Ping and S. Chen, *J. Mater. Chem. A*, 2017, **5**, 18261-18269.

Graphical Abstract
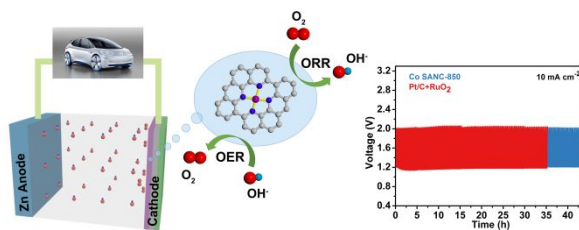
A scalable Co single-atom catalyst is fabricated by biomass complexation strategy, which exhibits high cycle efficiency in Zn-air battery.